

See discussions, stats, and author profiles for this publication at: <https://www.researchgate.net/publication/240475214>

Crystal Structure and Low-Temperature Magnetic Ordering in Rare Earth Iron Germanates $\text{LnFeGe}_2\text{O}_7$, Ln: Y, Pr, Dy, Tm, and Yb

ARTICLE in CHEMISTRY OF MATERIALS · MAY 2002

Impact Factor: 8.35 · DOI: 10.1021/cm0111332

CITATIONS

9

READS

41

4 AUTHORS, INCLUDING:



Concepción Cascales

Spanish National Research Council

212 PUBLICATIONS 2,533 CITATIONS

SEE PROFILE



Angeles Monge

Spanish National Research Council

441 PUBLICATIONS 6,762 CITATIONS

SEE PROFILE



Lauro Bucio

Universidad Nacional Autónoma de México

90 PUBLICATIONS 386 CITATIONS

SEE PROFILE

Crystal Structure and Low-Temperature Magnetic Ordering in Rare Earth Iron Germanates RFeGe_2O_7 , $\text{R} = \text{Y, Pr, Dy, Tm, and Yb}$

C. Cascales,^{*,†} M. T. Fernández-Díaz,^{†,‡} M. A. Monge,[†] and L. Bucio[§]

Instituto de Ciencia de Materiales de Madrid, CSIC. Cantoblanco, E-28049 Madrid, Spain, Institut Laue-Langevin, BP 156 X, F-38042 Grenoble Cedex, France, and Departamento de Estado Sólido, Instituto de Física, UNAM. Aptdo. Postal 20-364, 01000 Mexico D.F., México

Received May 23, 2001. Revised Manuscript Received February 21, 2002

Polycrystalline samples of iron and rare earth germanates, RFeGe_2O_7 ($\text{R} = \text{Y, Pr, Dy, Tm, and Yb}$), have been prepared. Depending on the size of R, they present two different monoclinic crystal structures, described either in space group $P2_1/c$ (no. 14) for $\text{R} = \text{Pr}$ or in $P2_1/m$ (no. 11) for the smaller rare earths $\text{R} = \text{Y, Dy, Tm, and Yb}$. The results of crystal structure refinements from room-temperature high-resolution neutron powder diffraction (NPD) data are given. Magnetization measurements between 350 and 1.6 K reveal the existence of one maximum, at 3 or 38 K for the praseodymium or yttrium germanate, respectively, and two separate anomalies for the remaining materials, which appear at T_1 and T_2 ($T_2 < T_1$), where $T_1 \approx 40$ K and $T_2 = 24, 6,$ and 5 K, for $\text{R} = \text{Dy, Tm, and Yb}$, respectively, indicating transitions to antiferromagnetically (AF) ordered states. Judging from low-temperature NPD data, three-dimensional (3D) AF ordering is established for all compounds, with simultaneous ordering of the R^{3+} and (or) Fe^{3+} ($\text{R} = \text{Y}$) sublattices, at 3 K in $\text{PrFeGe}_2\text{O}_7$, 38 K in YFeGe_2O_7 , and at $T_N = T_1$ for the remaining compounds. The ordered magnetic structure of $\text{PrFeGe}_2\text{O}_7$ can be described in terms of the propagation vector $\mathbf{k} = [1/2, 1/2, 0]$ and a model that consists of ferromagnetic coupling of the magnetic moments of Fe^{3+} and Pr^{3+} along the $-\text{FeO}_5-\text{PrO}_9-\text{FeO}_5-$ chains in the c direction, whereas along the two other axes, the moments show AF coupling. For the $\text{R} = \text{Y, Dy, Tm, and Yb}$ compounds, the propagation vector of the magnetic structures is $\mathbf{k} = [0, 0, 0]$. In each case, the magnetic structure consists of a ferromagnetic arrangement of all R^{3+} and (or) Fe^{3+} ($\text{R} = \text{Y}$) magnetic moments within one ac plane, whereas the corresponding moments in up and down adjacent planes are oppositely aligned, leading to 3D AF coupling along the b direction.

Introduction

Germanates of the form RMGe_2O_7 in which R represents trivalent rare earth elements and M represents the trivalent metals Al, Ga, and Fe constitute an interesting host among single-centered self-activated laser materials.^{1–3} Those with $\text{M} = \text{Al}$ or Ga and $\text{R} = \text{La–Dy}$ were found^{4,5} to present the monoclinic $\text{NdAlGe}_2\text{O}_7$ structure (space group $P2_1/c$). Studies of optical absorption, luminescence, and stimulated emission for Nd^{3+} ,⁵ as well as studies on crystal-field effects in RGaGe_2O_7 for $\text{R} = \text{Pr}^{3+}$ and Nd^{3+} ,^{6,7} have been carried out. In the iron family, depending on the size of R, phase formation

corresponds to the mentioned⁵ monoclinic type, I, for the larger R cations, i.e., those from La to Gd, and to the YFeGe_2O_7 structure type, II, described by the authors⁸ in the space group $P2_1/m$ (no. 11), for the smaller rare earth elements including Y and those from Tb to Yb. These structures present important differences, and the precise determination of their crystal data is the first step in developing a confident understanding of d–f interactions, mainly dealing with optical and magnetic features. Some results concerning magnetic properties have been previously reported,^{9,10} including the determination of the magnetic structures for a few compounds with the YFeGe_2O_7 structure type.^{8,11} In contrast, for iron and larger-R-containing

* To whom correspondence should be addressed. Fax: 34 91 3720623. E-mail: ccascales@icmm.csic.es.

[†] Instituto de Ciencia de Materiales de Madrid.

[‡] Present address: Institut Laue-Langevin.

[§] Departamento de Estado Sólido.

(1) Kaminskii, A. A. *Crystalline Lasers: Physical Processes and Operating Schemes*; CRC Press: Boca Raton, FL, 1996.

(2) Zaldo, C.; Rico, M.; Cascales, C.; Pujol, M. C.; Massons, J.; Aguiló, M.; Díaz, F.; Porcher, P. *J. Phys.: Condens. Matter* **2000**, *12*, 8531.

(3) Cascales, C.; Zaldo, C.; Caldiño, U.; García Solé, J.; Luo, Z. D. *J. Phys.: Condens. Matter* **2001**, *13*, 8071.

(4) Jarchow, O.; Klaska, K.-H.; Schenk-Strauss, H. Z. *Kristallogr.* **1985**, *172*, 159.

(5) Kaminskii, A. A.; Mill, B. V.; Butashin, A. V.; Belokoneva, E. L.; Kurbanov, K. *Phys. Status Solidi* **1987**, *103*, 575.

(6) Lozano, G.; Cascales, C.; Zaldo, C.; Porcher, P. *J. Alloys Compd.* **2000**, *303–304*, 349.

(7) Cascales, C.; Lozano, G.; Zaldo, C.; Porcher, P. *Chem. Phys.* **2000**, *257*, 49.

(8) Cascales, C.; Bucio, L.; Gutiérrez Puebla, E.; Rasines, I.; Fernández Díaz, M. T. *Phys. Rev. B* **1998**, *57*, 5240.

(9) Kazei, Z. A.; Kuyanov, Z. A.; Levitin, R. Z.; Markosyan, A. S.; Mill, B. V.; Reiman, S. Y.; Snegirev, V. V.; Tamazyan, S. A. *Sov. Phys. Solid State* **1989**, *31*, 233.

(10) Bucio, L.; Cascales, C.; Alonso, J. A.; Rasines, I. *J. Phys.: Condens. Matter* **1996**, *8*, 2641.

(11) Cascales, C.; Gutiérrez Puebla, E.; Klimin, S.; Lebech, B.; Monge, A.; Popova, M. N. *Chem. Mater.* **1999**, *11*, 2520.

germanates, the nature of the low-temperature ordered phase has not yet been described.

The aim of this article is therefore to characterize the microscopic magnetic behavior of RFeGe_2O_7 compounds, where $\text{R} = \text{Pr}$, Y , Dy , Tm , and Yb . Their syntheses and the refinement of their crystal structures, as well as low-temperature neutron diffraction studies, were undertaken to investigate the nature of the anomalies displayed by magnetic measurements. The magnetic structure of low-temperature phases is established, and finally, the relationship between crystal structure and magnetic order, as well as the role played by the identity of R , is discussed for the two kinds of materials.

Experimental Section

Preparation of Samples. RFeGe_2O_7 samples ($\text{R} = \text{Y}$, Pr , Dy , Tm , and Yb) were prepared as polycrystalline powder materials by solid-state reaction from analytical-grade mixtures of the stoichiometrically required amounts of Fe_3O_4 , GeO_2 , and Pr_6O_{11} or R_2O_3 , with a slight excess of the germanium oxide to counteract losses, especially as a vitrified product. Zirconia LECO 528-018 crucibles were employed. Samples were ground and heated in air to final temperatures between 1200 and 1250 °C, with higher temperatures being used for the heavier- R compounds, for two weeks with intermediate regrinding. Standard X-ray powder diffraction analysis indicated that the final samples were well-crystallized and appeared, within the limits of the technique, to be free of other crystalline phases.

Crystal and Magnetic Structure Refinements. Neutron powder diffraction (NPD) patterns were collected on the D1B and D2B powder diffractometers at the ILL-Grenoble, using wavelengths of 2.524 and 1.595 Å, respectively. About 8 g of sample contained in a cylindrical vanadium can was used in each case. The high flux and medium resolution of D1B were employed to study the thermal evolution of these materials in the temperature ranges 1.6–50 K for $\text{R} = \text{Y}$, Dy , Tm , and Yb and 1.6–20 K for $\text{R} = \text{Pr}$, with the vanadium can being held in a liquid helium cryostat. The diffraction patterns were typically collected every 1 K (0.5 K for $\text{PrFeGe}_2\text{O}_7$) in the angular range $5^\circ \leq 2\theta \leq 85^\circ$ in steps of $0.2^\circ 2\theta$. For the Dy-containing material, a concentric double-walled can was used to minimize the high absorption cross-section of Dy and, hence, of the material. To obtain more accurate data, the lowest-temperature pattern consisted of the integration of several measured patterns at 1.6 K. The high-resolution D2B diffractometer was used to obtain more extensive and accurate data at room temperature over the large angular range $5^\circ \leq 2\theta \leq 155^\circ$ in steps of $0.05^\circ 2\theta$.

The Rietveld method was used to refine the crystal and magnetic structures. All of the data were analyzed with the program WinPLOTR.¹² A pseudo-Voigt function was chosen to generate the line shape of the diffraction peaks. The background was fitted to a polynomial refinable function. Crystal structures of the RFeGe_2O_7 materials for $\text{R} = \text{Y}$, Dy , Tm , and Yb at room temperature were refined taking as starting parameters those previously obtained for $\text{TbFeGe}_2\text{O}_7$.⁸ Crystal data at room temperature of $\text{PrFeGe}_2\text{O}_7$ were those previously reported.¹⁰ D1B diffraction patterns taken at increasing temperatures were refined sequentially, with the starting parameters for each pattern being those resulting from the preceding refinement one at lower temperature. The atomic coordinates for all atoms were fixed to the values obtained with the high-resolution pattern in these variable-temperature refinements.

Magnetic Measurements. A SQUID magnetometer (Quantum Design) operating from 350 to 1.7 K at 100 Oe was used

to carry out dc magnetic susceptibility measurements. Diamagnetic corrections¹³ for the magnetic susceptibilities were taken into account.

Crystal Structures in RFeGe_2O_7

Phase formation in the RFeGe_2O_7 family depends on the size of R . The structure corresponds to the monoclinic type $P2_1/c$,^{4,5,10} I, for the larger R cations, i.e., those from La to Gd, and the YFeGe_2O_7 structure type, II, described by the authors⁸ in the space group $P2_1/m$ (no. 11), for the smaller rare earth elements including Y and those from Tb to Yb. The two structural types present important differences when their coordination polyhedra, especially those of R and iron cations, and the connectivities between all of the atoms are compared. In I- RFeGe_2O_7 , chains of edge-sharing flexed RO_9 -tricapped trigonal prisms lie along the a axis, being linked alternately through an edge or a corner of isolated distorted FeO_5 trigonal bipyramids in the c direction, and the two kinds of GeO_4 tetrahedra are associated by corner sharing to form diortho Ge_2O_7 groups along the $[001]$ direction. II- RFeGe_2O_7 contains three kinds of coordination polyhedra: distorted FeO_6 octahedra joined in pairs by edge sharing, RO_7 -capped octahedra, and four kinds of Ge atoms exhibiting the usual tetrahedral coordination, also associated by sharing corners to form isolated diortho Ge_2O_7 groups. Layers made up of flattened chains of RO_7 polyhedra along the b axis and pairs of FeO_6 , which link these chains in the c direction, run parallel to the bc crystal plane. Ge_2O_7 units are not connected in either the a or b direction, but they play a bridging role between parallel RO_7 - and FeO_6 -containing layers. Figure 1a and b illustrates the mentioned details of these structures.

Table 1 summarizes the structural parameters for RFeGe_2O_7 ($\text{R} = \text{Y}$, Dy , Tm , and Yb) from NPD data collected at room temperature on D2B. Lattice parameters for $\text{PrFeGe}_2\text{O}_7$ ¹⁰ are also included in this table as they represent the starting point for the analysis of the low-temperature magnetic structure. The current final refined positional and displacement parameters are given in Table 2, and Table 3 lists the main interatomic distances. Figure 2 shows observed and calculated room-temperature NPD profiles for $\text{TmFeGe}_2\text{O}_7$, which was chosen as a representative example of the II- RFeGe_2O_7 compounds.

Magnetic Susceptibility Measurements

Figure 3 shows the variation with temperature of the molar magnetic susceptibility, χ_m , for $\text{PrFeGe}_2\text{O}_7$. A clear maximum appears at very low temperature, 3.2 K, that is related to the transition to an AF ordered state of the magnetic cations. For temperatures from 50 K to room temperature, a Curie–Weiss law is observed, such that $\chi_m^{-1} = 47.8(7) + 0.697(4) T \text{ mol} \cdot \text{emu}^{-1}$ ($r = 0.999$), with $\Theta_c = -69$ K and $\mu_{\text{eff}} = 3.4 \mu_B$. A comparison with the magnetic behavior of an isostructural compound for which only the magnetic subsystem of Fe^{3+} cations exists can be established with the previously measured χ vs T data for $\text{LaFeGe}_2\text{O}_7$.¹⁰ This plot presents a slight deviation from linearity over the

(12) Roisnel, T.; Rodríguez Carvajal, J. *WinPLOTR Program for Rietveld Refinement and Pattern Matching Analysis*; Laboratoire Léon Brillouin, CEA-CNRS, Centre d'Etudes de Saclay: Gif-sur-Yvette, France, 1999.

(13) Boudreaux, E. A.; Mulay, L. N. *Theory and Applications of Molecular Paramagnetism*; Wiley: New York, 1976; pp 494–495.

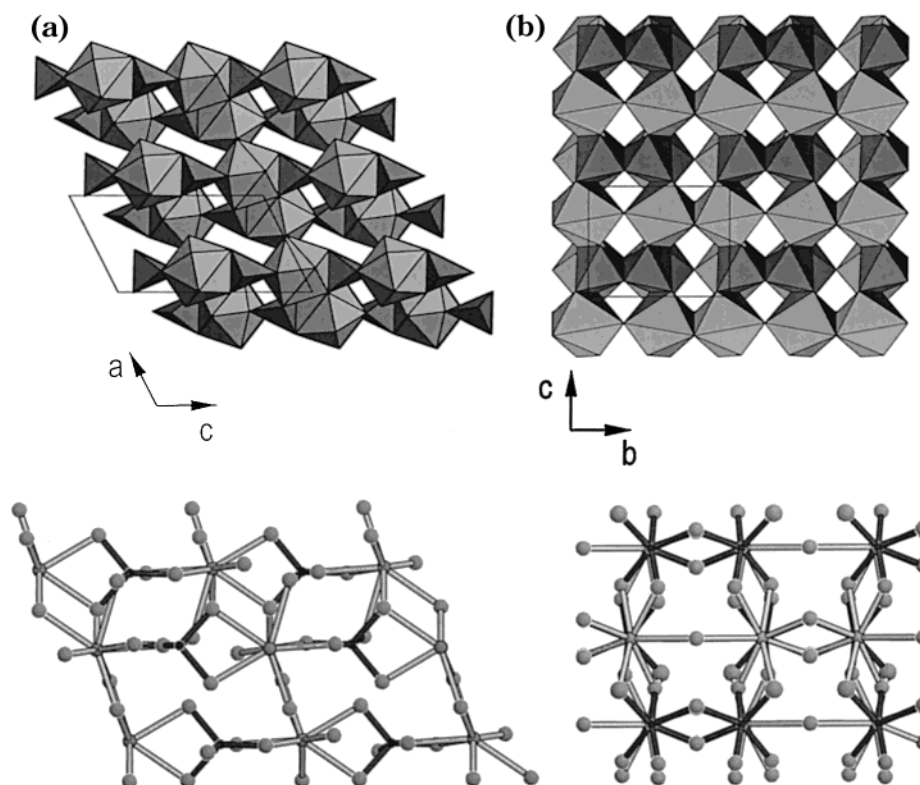


Figure 1. (a) Projection onto the ac plane of the $I\text{-}R\text{FeGe}_2\text{O}_7$ structure. Large (gray) and small (dark gray) polyhedra correspond to RO_9 -tricapped trigonal prisms and FeO_5 trigonal bipyramids, respectively. (b) Projection of the crystal structure of $II\text{-}R\text{FeGe}_2\text{O}_7$ onto the bc plane, depicting the RO_7 (gray) chains along the b axis linked in the c direction through pairs of FeO_6 (dark gray) octahedra. Connectivity between R and Fe polyhedra is shown, in each case, by a ball-and-stick representation. In both cases, the positions of Ge atoms are omitted.

Table 1. Lattice Parameters and Reliability Factors for $R\text{FeGe}_2\text{O}_7$, $R = \text{Y, Pr, Dy, Tm, and Yb}$, from Neutron Diffraction Data (D2B ILL) at Room Temperature

	Y^a	Pr^b	Dy^a	Tm^a	Yb^a
lattice parameters					
a (Å)	9.6544(3)	7.2422(7)	9.6400(5)	9.6557(4)	9.6672(4)
b (Å)	8.5207(2)	6.6361(6)	8.4753(4)	8.5444(4)	8.5558(3)
c (Å)	6.6737(2)	12.986(1)	6.7122(3)	6.6336(3)	6.6253(3)
β (°)	100.741(2)	117.13(5)	100.515(3)	101.125(4)	101.321(3)
V (Å ³)	539.37(3)	555.44(1)	539.19(5)	537.00(4)	537.32(4)
no. of reflections	1148	679	1144	1147	1146
R_{wp}	6.11	2.66	6.61	7.39	8.56
R_{exp}	1.17	1.12	6.23	2.22	2.37
R_{Bragg}	5.83	3.19	6.33	9.75	10.9
R_f	4.03	1.99	3.86	6.88	7.37

^a Space group $P2_1/m$ (no. 11). ^b Space group $P2_1/c$ (no. 14); data from ref 10.

whole measured range, with a magnetic moment becoming smaller as the temperature decreases and no maximum being observed at low temperature.

A qualitative difference is observed when the plot of $\text{PrFeGe}_2\text{O}_7$ is compared with the curves for $II\text{-}R\text{FeGe}_2\text{O}_7$ compounds. With the exception of the yttrium germanate, for which only one maximum in $\chi_m(T)$ occurs at 38 K,⁸ the data collected at lower temperatures reveal the presence of two different anomalies in the variation of χ_m (more visible in the derivative of the product $\chi_m T$ with respect to T), which can be attributed to transitions to AF ordered states. In each case, apart from clear peaks at $T_2 = 24, 6,$ and 5 K for $R = \text{Dy, Tm, and Yb}$, respectively, there is another maximum, at higher temperature T_1 , consisting of a smaller peak around 40 K in all cases. Up ~ 60 to room temperature, Curie–

Weiss behavior is followed for these compounds, such that $\chi_m^{-1} = 0.943(11) + 0.06951(5)T$, $16.3(4) + 0.324(3)T$, and $77(1) + 0.678(8)T$ mol $\cdot\text{emu}^{-1}$ ($r = 0.9999, 0.998,$ and 0.996 , respectively), with paramagnetic Curie temperatures $\Theta_c = -13.6, -50,$ and -114 K and effective magnetic moments $\mu_{\text{eff}} = 10.8, 5.0,$ and $3.5 \mu_B$ for $R = \text{Dy, Tm, and Yb}$ materials, respectively. Figures 4 and 5 display the temperature dependence of χ_m for $R = \text{Tm and Yb}$ compounds.

Magnetic Ordering in $R\text{FeGe}_2\text{O}_7$

The evolution of the NPD patterns for $\text{PrFeGe}_2\text{O}_7$, in the range of 2θ scattering angle from 10° to 87° and temperatures from 1.5 to 4 K is presented in Figure 6. A series of not very strong extra peaks appears below 3 K, the temperature that corresponds to the observed maximum in the χ_m vs T curve. The newly observed peaks provide an indication of the three-dimensional (3D) AF order of the Pr^{3+} and Fe^{3+} networks at very low temperature. In the lowest-temperature NPD pattern of $\text{PrFeGe}_2\text{O}_7$, all observed peaks can be indexed within a commensurate lattice with unit cell parameters $a' = 2a, b' = 2b, c' = c$, and $\beta' = \beta$, where a, b, c , and β are the parameters of the crystallographic unit cell. In contrast, a careful analysis and comparison of collected data for isostructural $\text{LaFeGe}_2\text{O}_7$ at temperatures between 1.6 and 20 K did not reveal any signs of magnetic Bragg reflections associated with the ordering of the Fe^{3+} magnetic moments.

The evolution from 1.6 to ~ 75 K of the NPD patterns of $II\text{-}R\text{FeGe}_2\text{O}_7$ compounds, for $10\text{--}85^\circ$ in 2θ , shows in each case a series of extra peaks appearing below 40

Table 2. Final Refined Positional and Thermal Parameters from NPD at Room Temperature for RFeGe₂O₇, R = Y, Dy, Tm, and Yb^a

	<i>x/a</i>	<i>y/b</i>	<i>z/c</i>	<i>B</i> (Å ²)	<i>x/a</i>	<i>y/b</i>	<i>z/c</i>	<i>B</i> (Å ²)
R = Y					R = Dy			
R	0.755(1)	0.5459(4)	0.7501(2)	0.68(8)	0.743(1)	0.5382(4)	0.749(1)	0.35(8)
Ge1	0.525(1)	0.75	0.055(2)	0.52(6)	0.526(2)	0.75	0.043(4)	0.4(1)
Ge2	0.554(1)	0.25	0.491(1)	0.52(6)	0.549(2)	0.25	0.463(2)	0.4(1)
Ge3	0.948(1)	0.25	0.033(1)	0.52(6)	0.948(2)	0.25	−0.001(2)	0.4(1)
Ge4	0.033(1)	0.25	0.547(2)	0.52(6)	0.029(2)	0.25	0.553(4)	0.4(1)
Fe	0.749(1)	0.4503(4)	0.250(1)	0.84(6)	0.750(2)	0.4465(7)	0.253(3)	0.6(1)
O1	0.647(1)	0.418(1)	0.484(1)	0.92(4)	0.633(2)	0.433(2)	0.457(3)	0.63(8)
O2	0.886(2)	0.25	0.346(3)	0.92(4)	0.879(4)	0.25	0.358(5)	0.63(8)
O3	0.946(1)	0.25	0.748(2)	0.92(4)	0.933(3)	0.25	0.736(3)	0.63(8)
O4	0.5849(6)	0.25	0.754(2)	0.92(4)	0.560(3)	0.25	0.734(3)	0.63(8)
O5	0.861(1)	0.067(1)	0.038(1)	0.92(4)	0.861(2)	0.082(2)	0.025(3)	0.63(8)
O6	0.124(2)	0.25	0.158(2)	0.92(4)	0.125(3)	0.25	0.141(5)	0.63(8)
O7	0.137(1)	0.076(1)	0.553(1)	0.92(4)	0.146(2)	0.092(2)	0.544(3)	0.63(8)
O8	0.382(2)	0.25	0.361(2)	0.92(4)	0.387(3)	0.25	0.350(4)	0.63(8)
O9	0.617(2)	0.25	0.147(2)	0.92(4)	0.621(4)	0.25	0.149(5)	0.63(8)
O10	0.634(1)	0.5990(9)	0.044(1)	0.92(4)	0.629(2)	0.582(2)	0.045(3)	0.63(8)
R = Tm					R = Yb			
R	0.753(2)	0.5519(8)	0.755(3)	1.1(1)	0.7547(9)	0.5498(5)	0.744(1)	0.68(8)
Ge1	0.525(2)	0.75	0.055(2)	0.60(8)	0.524(1)	0.75	0.060(2)	0.62(7)
Ge2	0.552(2)	0.25	0.473(2)	0.60(8)	0.555(1)	0.25	0.495(2)	0.62(7)
Ge3	0.947(2)	0.25	0.004(2)	0.60(8)	0.948(1)	0.25	0.032(2)	0.62(7)
Ge4	0.033(2)	0.25	0.549(3)	0.60(8)	0.035(1)	0.25	0.539(2)	0.62(7)
Fe	0.752(1)	0.4524(6)	0.246(2)	0.6(1)	0.747(1)	0.4508(7)	0.258(2)	0.6(1)
O1	0.644(2)	0.407(1)	0.489(2)	1.26(7)	0.647(1)	0.433(1)	0.465(2)	0.97(6)
O2	0.878(2)	0.25	0.331(3)	1.26(7)	0.876(2)	0.25	0.346(3)	0.97(6)
O3	0.955(2)	0.25	0.742(3)	1.26(7)	0.966(1)	0.25	0.769(3)	0.97(6)
O4	0.590(2)	0.25	0.761(3)	1.26(7)	0.578(2)	0.25	0.767(2)	0.97(6)
O5	0.852(2)	0.062(1)	0.033(2)	1.26(7)	0.856(1)	0.095(2)	0.008(2)	0.97(6)
O6	0.111(3)	0.25	0.139(3)	1.26(7)	0.120(2)	0.25	0.140(3)	0.97(6)
O7	0.141(2)	0.077(2)	0.546(3)	1.26(7)	0.146(1)	0.097(2)	0.541(2)	0.97(6)
O8	0.373(2)	0.25	0.346(3)	1.26(7)	0.393(2)	0.25	0.357(3)	0.97(6)
O9	0.611(2)	0.25	0.136(3)	1.26(7)	0.615(2)	0.25	0.170(3)	0.97(6)
O10	0.635(2)	0.597(2)	0.049(3)	1.26(7)	0.629(1)	0.573(1)	0.058(2)	0.97(6)

^a Isotropic displacement parameters for Ge and O atoms were constrained to the same values in all compounds.

K. These peaks correspond to transitions to 3D AF ordered states of 4f³⁺ and (or) Fe³⁺ (R = Y) subcells in the studied materials. The intensities of the magnetic reflections grow regularly to reach the maximum at 1.6 K, this maximum getting less intense from the Dy to the Yb compound. Figures 7 and 8 depict the evolution with temperature of the NPD patterns for TmFeGe₂O₇ and YbFeGe₂O₇, respectively. Below ~40 K, all observed Bragg peaks can be indexed within a commensurate lattice with approximately the same unit cell parameters as the crystallographic one. Because “pure magnetic” reflections are those indexed to 0*k*0 (where 0*k*0 for *k* = 2*n* + 1 is an extinction condition for *P*₂₁/*m*), some ordering of the magnetic moments perpendicular to the *b* axis can be initially surmised.¹⁴

Group Theory Analyses for PrFeGe₂O₇ and II–RFeGe₂O₇, with R = Y, Dy, Tm, and Yb

The nuclear unit cell of PrFeGe₂O₇ contains four Pr³⁺ and four Fe³⁺ cations, located at the general positions 4e, (*x*, *y*, *z*), (−*x*, *y* + 1/2, 1/2 − *z*), (−*x*, −*y*, −*z*), and (*x*, 1/2 − *y*, *z* + 1/2), related by the symmetry operations of the space group *P*₂₁/*c*. The magnetic structure can be described by considering the magnetic moments of these atoms, and the remaining ones can be deduced by means of the *t*_N Bravais translation vector, according to *m*_{*j*N} = *m*_{*j*0}*e*^{−2π*i**k**t*_N}. Because of the above-indicated relationship

between the unit cell parameters of the magnetic and nuclear lattices, this low-temperature 3D long-range-ordered magnetic structure can be described in terms of a single propagation vector **k** = [1/2, 1/2, 0].

Possible magnetic structures compatible with the crystal symmetry can be obtained from group-theory analysis.¹⁵ All possible forms of ordering of the magnetic moments are determined through the base functions of the irreducible representations of the wave vector group *G*_{*k*}, which contains only those symmetry operations of the high-temperature space-group (*T* > *T*_N) that leave the propagation vector invariant or transform it into an equivalent vector.

For PrFeGe₂O₇, the symmetry operations to be considered are {*E*, *C*₂, *I*, *c*}, representing identity, a binary axis along *b*, inversion, and a glide plane, respectively. The transformation properties of the components of the magnetic moments under the symmetry operations of the group *G*_{*k*} (*C*_{2*h*}) associated with *P*₂₁/*c* define a reducible representation *Γ* made up of four matrices whose traces are 12, 0, 0, and 0 for the four symmetry elements. Table 4 gives the characters of the irreducible representations *Γ*^{*ν*} of *G*_{*k*}, and Table 5 lists the transformation rules of the magnetic moment components under the symmetry operations. The irreducible representations contained in *Γ* (for Pr³⁺ and Fe³⁺) are, in both cases, 3A_g + 3B_g + 3A_u + 3B_u. Because only vectors belonging to the same representation for the two kind of atoms,

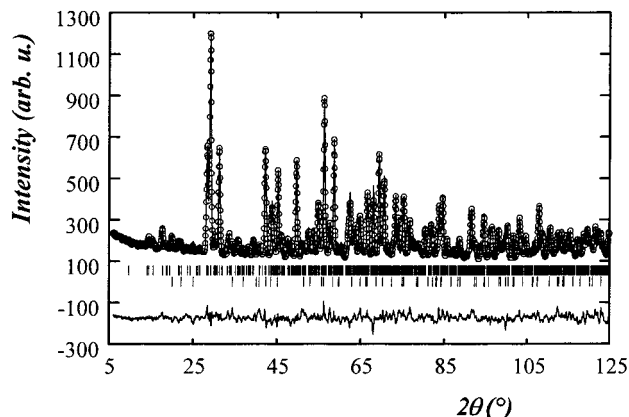
(14) Bacon, G. E. *Neutron Diffraction*; Oxford University Press: New York, 1975.

(15) Bertaut, E. F. *Acta Crystallogr. A* **1968**, *24*, 217.

Table 3. Main Interatomic Distances (Å) in $R\text{FeGe}_2\text{O}_7$, $R = \text{Y, Dy, Tm, and Yb}^a$

	Y	Dy	Tm	Yb
R–O(1)	2.18(1)	2.24(2)	2.26(2)	2.18(1)
R–O(4)	3.008(9)	3.01(2)	3.04(1)	3.10(1)
R–O(5)	2.22(1)	2.23(2)	2.12(2)	2.21(1)
R–O(6)	2.12(1)	2.25(2)	2.13(2)	2.15(1)
R–O(7)	2.46(1)	2.45(2)	2.44(2)	2.31(2)
R–O(8)	2.22(1)	2.22(2)	2.19(2)	2.25(1)
R–O(10)	2.49(1)	2.47(2)	2.47(2)	2.61(2)
Fe–O(1)	2.01(1)	1.93(3)	2.10(2)	1.83(2)
Fe–O(2)	2.18(1)	2.12(3)	2.18(2)	2.14(2)
Fe–O(5)	1.94(1)	2.04(3)	1.89(2)	2.16(2)
Fe–O(7)	1.89(1)	1.97(3)	1.91(2)	1.97(2)
Fe–O(9)	2.16(1)	2.12(3)	2.14(2)	2.15(2)
Fe–O(10)	2.04(1)	2.01(3)	1.99(2)	1.88(2)
Ge(1)–O(4)	1.80(1)	1.84(3)	1.86(2)	1.65(2)
Ge(1)–O(9)	1.74(2)	1.73(4)	1.77(3)	1.82(3)
Ge(1)–O(10) × 2	1.68(1)	1.74(2)	1.66(2)	1.83(1)
Ge(2)–O(1) × 2	1.70(1)	1.75(2)	1.62(2)	1.83(1)
Ge(2)–O(4)	1.72(1)	1.80(3)	1.85(2)	1.77(2)
Ge(2)–O(8)	1.73(2)	1.60(3)	1.70(3)	1.65(2)
Ge(3)–O(3)	1.89(1)	1.75(2)	1.77(2)	1.79(2)
Ge(3)–O(5) × 2	1.77(1)	1.68(2)	1.82(1)	1.59(2)
Ge(3)–O(6)	1.75(2)	1.79(3)	1.72(3)	1.68(3)
Ge(4)–O(2)	1.76(2)	1.76(4)	1.78(3)	1.79(3)
Ge(4)–O(3)	1.71(2)	1.66(3)	1.54(2)	1.78(2)
Ge(4)–O(7) × 2	1.79(1)	1.76(2)	1.82(2)	1.70(2)
R–R, <i>b</i>	3.478(5)	3.590(5)	3.398(8)	3.425(6)
Fe–Fe, <i>b</i>	5.042(5)	4.885(5)	5.147(9)	5.131(6)
Fe–Fe, <i>c</i>	3.413(4)	3.331(8)	3.433(7)	3.435(8)
R–Fe, <i>c</i>	5.108(4)	5.144(8)	5.112(7)	5.121(8)
	3.43(1)	3.43(2)	3.54(2)	3.32(1)
	3.44(1)	3.46(2)	3.31(2)	3.52(1)

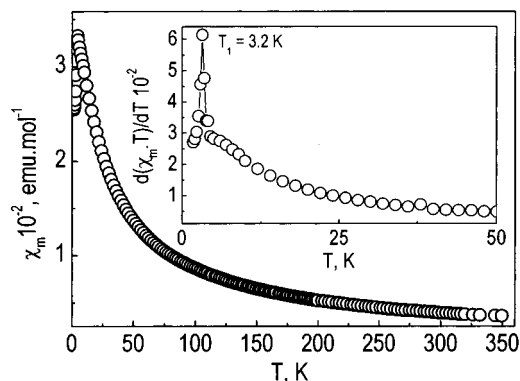
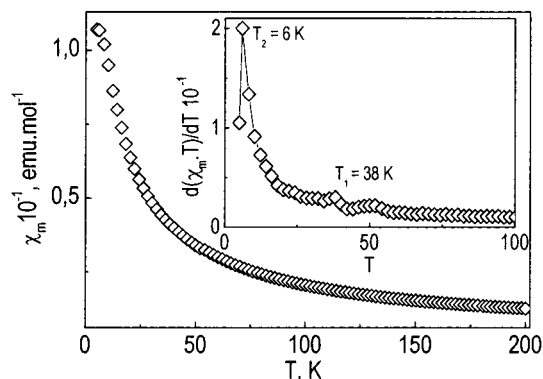
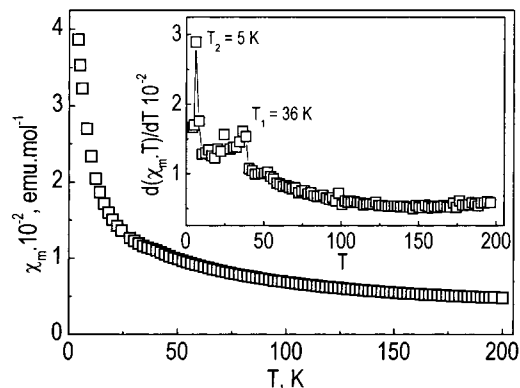
^a Interatomic distances (Å) in $\text{PrFeGe}_2\text{O}_7$ are Pr–Pr = 4.039(22); Fe–Fe = 5.203(9); Pr–Fe = 3.452(14), 3.499(13), 5.041(14), 5.441(14).

**Figure 2.** Observed, calculated, and difference neutron diffraction (D2B, ILL) profiles of $\text{TmFeGe}_2\text{O}_7$ at room temperature. The vertical marks correspond to the positions of the allowed Bragg reflections for the crystallographic structure.

Pr^{3+} and Fe^{3+} , can be coupled, to a first approximation,¹⁵ four possibilities for the ordering of the magnetic moments of the two magnetic cells must be considered, each one defined by six free parameters, three for each magnetic lattice. These possible arrangements were analyzed by means of the basis functions obtained through the projection operator

$$\Psi_{\alpha}^{(\nu)} = \sum_j \chi_{\nu}(C_j) C_j m_{\alpha}$$

where $\Psi_{\alpha}^{(\nu)}$ is the basis function, $\chi_{\nu}(C_j)$ is the character of the irreducible representation ν corresponding to the C_j operation, and m_{α} is the α ($\alpha = x, y, z$) component of

**Figure 3.** Temperature dependence of the molar magnetic susceptibility χ_m for $\text{PrFeGe}_2\text{O}_7$. The inset shows the derivative of the product $\chi_m T$ with the temperature, $d(\chi_m T)/dT$.**Figure 4.** Temperature dependence of the molar magnetic susceptibility χ_m for $\text{TmFeGe}_2\text{O}_7$. The inset shows the derivative of the product $\chi_m T$ with the temperature, $d(\chi_m T)/dT$.**Figure 5.** Temperature dependence of the molar magnetic susceptibility χ_m for $\text{YbFeGe}_2\text{O}_7$. The inset shows the derivative of the product $\chi_m T$ with the temperature, $d(\chi_m T)/dT$.

a given magnetic moment. Corresponding sets of basis vectors for the four irreducible representations, for Pr^{3+} as well as for Fe^{3+} , are indicated in Table 6. Finally, the two potential kinds of coupling between the two types of magnetic cations, ferromagnetic (F) or antiferromagnetic (AF), must be also considered.

A detailed development of the group theory analysis for germanates with the $\text{II-RFeGe}_2\text{O}_7$ structure type can be found elsewhere.⁸ Ferromagnetic ($F_x = m_{\text{xFe}} + m_{\text{xR}}$, $F_z = m_{\text{zFe}} + m_{\text{zR}}$) or antiferromagnetic ($A_x = m_{\text{xFe}} - m_{\text{xR}}$, $A_z = m_{\text{zFe}} - m_{\text{zR}}$) couplings, derived from the B_g irreducible representation of Fe^{3+} and R^{3+} magnetic networks, are the only two distributions of magnetic moments to be considered for this group of materials.

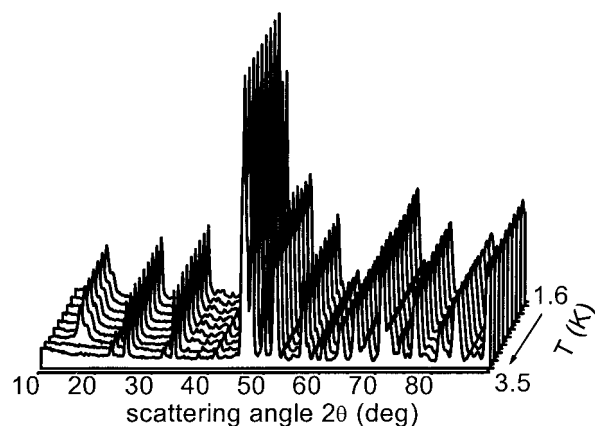


Figure 6. Evolution between 1.6 and 4 K of the neutron powder diffraction patterns of $\text{PrFeGe}_2\text{O}_7$.

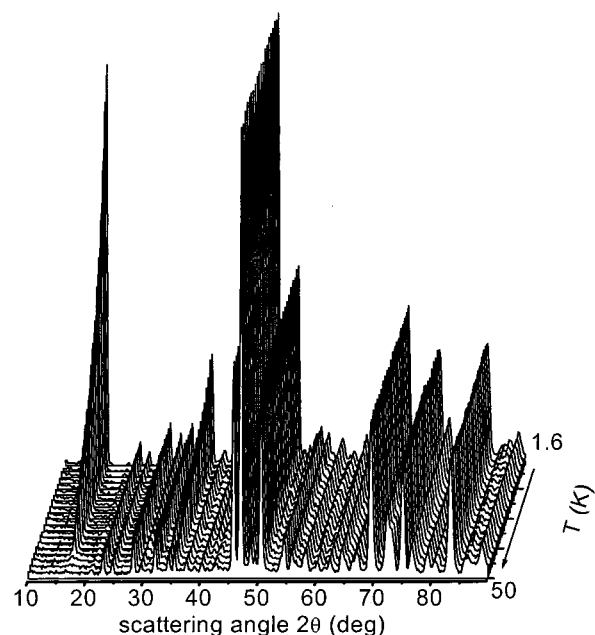


Figure 7. Evolution between 1.6 and 50 K of the neutron powder diffraction patterns of $\text{TmFeGe}_2\text{O}_7$.

Magnetic Structure Refinements

In the analysis of the low-temperature NPD data, a two-phase refinement for every temperature was performed. In each case, the crystal structure was refined taking as starting parameters those obtained at room temperature with high-resolution data. The magnetic structure was refined as an independent phase for which only magnetic atoms were defined. The scale and displacement parameters were constrained for both the nuclear and magnetic structures.

An independent long-range magnetic order for the network of Fe^{3+} cations in $\text{I-RFeGe}_2\text{O}_7$ compounds can be discarded as long as the measurements performed on the La compound hold, i.e., the absence of both one clear maximum in the χ vs T plot and magnetic reflections in the 1.6 K pattern of $\text{LaFeGe}_2\text{O}_7$. In fact, the failure to observe any magnetic signal is not surprising for a structure where *isolated* FeO_5 trigonal bipyramids are arranged between chains of LaO_9 polyhedra. Because a single transition temperature was observed from NPD as well as in magnetic susceptibility data for $\text{PrFeGe}_2\text{O}_7$, the analysis of its low temperature

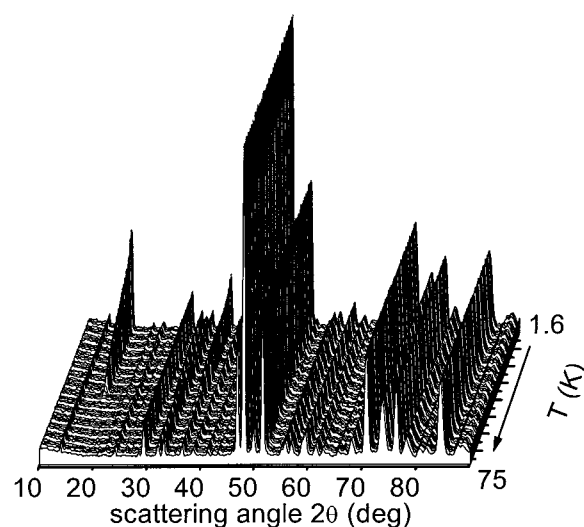


Figure 8. Evolution between 1.6 and 75 K of the neutron powder diffraction patterns of $\text{YbFeGe}_2\text{O}_7$.

Table 4. Character of the Irreducible Representations of G_k for $\text{PrFeGe}_2\text{O}_7$

	E	C_2	i	c
A_g	1	1	1	1
B_g	1	-1	1	-1
A_u	1	1	-1	-1
B_u	1	-1	-1	1

Table 5. Transformation Properties of the Components of the Magnetic Moments of Pr^{3+} and Fe^{3+} under the Symmetry Operations of G_k

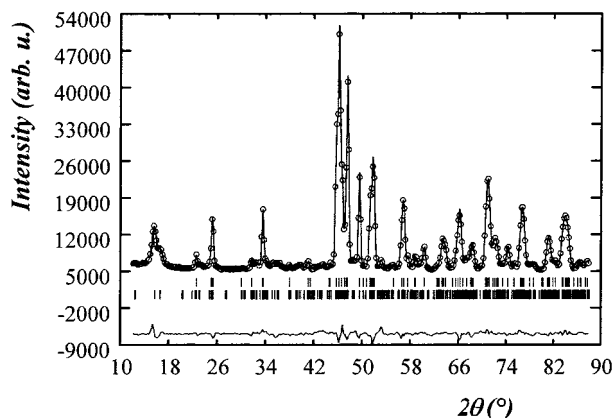
	E	C_2	i	c
x	1	-1	1	-1
y	1	1	1	1
z	1	-1	1	-1

pattern was started with a consideration of the order of the magnetic moments exclusively on the rare earth sites. However, experimental data at the lowest temperature can be satisfactorily fitted only if the magnetic moments in Fe^{3+} sites also become ordered. The best adjustment corresponds to the model given by the Γ^3 (A_u) representation, which establishes the collinear arrangement of x and z components of the magnetic moments of cations of the two pairs (1) and (4) as well as (2) and (3) (Pr^{3+} or Fe^{3+}), with the two pairs being oppositely aligned with each other in the ac plane but with the y component of the magnetic moments for (1) and (2) as well as for (3) and (4) cations being aligned for each pair and antiparallel between the two pairs. Moreover, the best model implies the ferromagnetic coupling between the two kinds of magnetic cells, i.e., the components of the magnetic moments of $\text{Pr}1$ and $\text{Fe}1$ are collinear. The final refinement therefore provides a 3D AF ordered magnetic structure consisting of ferromagnetic coupling of Pr^{3+} and Fe^{3+} magnetic moments in each chain lying along the c direction and the corresponding moments in the next parallel chain in the b direction being oppositely aligned, as imposed by the propagation vector. The arrangement of the magnetic moments of $-\text{PrO}_9-\text{FeO}_5-\text{PrO}_9-$ chains parallel to c is reversed for every fourth one of these consecutive chains along the a direction.

In Figure 9, the observed and final fit patterns for $\text{PrFeGe}_2\text{O}_7$ at 1.6 K are represented. Tables 7 and 8

Table 6. Basis Vectors of the Pr^{3+} and Fe^{3+} Sublattices of $\text{PrFeGe}_2\text{O}_7$ for the Four Irreducible Representations of G_k

	x	y	z
$\Gamma^1 A_g$	$m_{1x} - m_{2x} + m_{3x} - m_{4x}$	$m_{1y} + m_{2y} + m_{3y} + m_{4y}$	$m_{1z} - m_{2z} + m_{3z} - m_{4z}$
$\Gamma^2 B_g$	$m_{1x} + m_{2x} + m_{3x} + m_{4x}$	$m_{1y} - m_{2y} + m_{3y} - m_{4y}$	$m_{1z} + m_{2z} + m_{3z} + m_{4z}$
$\Gamma^3 A_u$	$m_{1x} - m_{2x} - m_{3x} + m_{4x}$	$m_{1y} + m_{2y} - m_{3y} - m_{4y}$	$m_{1z} - m_{2z} - m_{3z} + m_{4z}$
$\Gamma^4 B_u$	$m_{1x} + m_{2x} - m_{3x} - m_{4x}$	$m_{1y} - m_{2y} + m_{3y} - m_{4y}$	$m_{1z} + m_{2z} - m_{3z} - m_{4z}$

**Figure 9.** Neutron diffraction pattern of $\text{PrFeGe}_2\text{O}_7$ (D1B, ILL) at 1.6 K. The solid line is the calculated profile, and the vertical marks correspond to the positions of the Bragg reflections for the crystallographic (first row) and magnetic (second row) structures. The difference curve is plotted at the bottom of the figure.**Table 7. Lattice Parameters and Discrepancy Factors for FeRGe_2O_7 , $R = \text{Y, Pr, Dy, Tm, and Yb}$, from D1B–ILL Neutron Diffraction Data at 1.6 K**

	Y	Pr	Dy	Tm	Yb
lattice parameters					
a (Å)	9.616(2)	14.434 (2)	9.602(1)	9.642(2)	9.635(1)
b (Å)	8.481(2)	13.235 (1)	8.423(1)	8.547(2)	8.528(1)
c (Å)	6.652(1)	12.963 (1)	6.7013(1)	6.6366(9)	6.6074(8)
β (°)	100.698(9)	117.17(1)	100.39(1)	101.121(9)	101.352(8)
V (Å ³)	533.0(2)		533.1(1)	536.7(1)	532.3(1)
no. of reflections	210	810	179	198	189
reliability factors					
χ^2	30.7	11.1	5.90	62.9	10.1
R_{exp}	2.01	2.30	2.77	1.58	3.42
R_{Bragg}	5.33	3.51	3.03	6.69	5.11
R_t	4.52	2.08	2.61	5.36	4.59
R_{mag}	10.6	6.98	2.00	3.87	8.96

provide a summary of the refined structural parameters and magnetic moments at 1.6 K, respectively. The magnetic moments are written in the Cartesian components M_x , M_y , and M_z allowed by the magnetic structure, as well as in spherical coordinates, with φ and ϕ being the angles of M with respect to the x and z axes, respectively. The values of the ordered magnetic moments M , 2.9(2) for Pr^{3+} and 3.1(3) for Fe^{3+} , are lower than those expected for free ions, 3.2 and $5.9 \mu_B$ for Pr^{3+} and high-spin Fe^{3+} , respectively. Actually, the magnetic peaks in 1.6 K NPD spectra might have not yet reached their maximum intensities, and therefore, the reduction in M is not surprising, i.e., these values correspond to unsaturated magnetic moments.

For the group of iron germanates with smaller rare earths, the first performed magnetic structure refinement corresponds to YFeGe_2O_7 , with only a magnetic network of Fe^{3+} cations. The best fit of the experimental NPD data at 1.6 K, with the model provided by the B_g representation, is described through the x and z components of the magnetic moments of Fe^{3+} cations. The

magnetic structure consists of a ferromagnetic arrangement of Fe^{3+} magnetic moments, whose directions form a small angle with the *negative* direction of the c axis within one ac plane (Table 8), while the moments in the up and down perpendicular to b adjacent planes are oppositely aligned, leading to 3D AF coupling along the b direction.

For the remaining $R = \text{Dy, Tm, and Yb}$ compounds of this group, final refinements of the low-temperature NPD data conduct to establish the ordered magnetic structures, also associated with the model of the B_g irreducible representation. They consist of ferromagnetic coupling between the magnetic moments of all Fe^{3+} and R^{3+} ions within every ac plane, with the coupling between parallel ac planes being AF along the b direction.

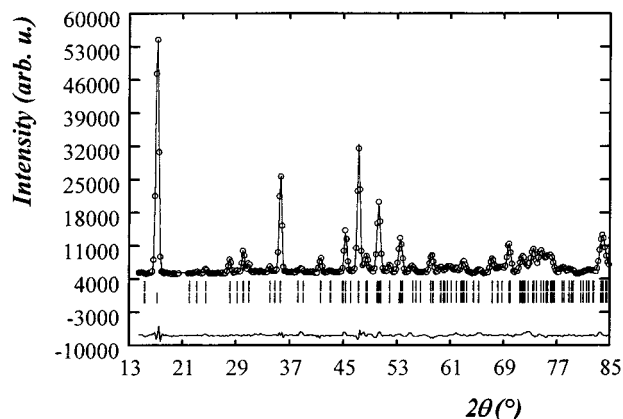
In Figure 10, the observed and final refined patterns at 1.6 K for $\text{DyFeGe}_2\text{O}_7$ are presented. Tables 7 and 8 also include a summary of the refined structural parameters and magnetic moments at this temperature for the $R = \text{Y, Dy, Tm, and Yb}$ compounds. Higher values found for χ^2 are mainly associated with the high flux of D1B neutron diffractometer, with some hundreds of thousands of counts experimentally collected in each step. Because χ^2 basically represents a summation of the square differences between experimentally observed and calculated counts over the whole measured 2θ range,¹² its final value ends up being somewhat elevated in some cases. Still, the remaining reliability factors, already normalized, present homogeneously lower values.

The last table indicates that the magnetic structure is the same for the four compounds but that the orientations of their magnetic moments are very dependent on the considered rare earth. Thus, whereas for both Y- and Yb-containing materials the magnetic moments of the $-\text{RO}_7-\text{FeO}_6-\text{RO}_7-$ chains that are parallel to c can be viewed as being nearly aligned (especially for the Yb^{3+} network) along the negative direction of the c axis, for $\text{TmFeGe}_2\text{O}_7$, the moments (mainly of Fe^{3+} cations) are turned and can be regarded as lying closer to the a axis than to the c axis. Figure 11 shows schematic views of the disposition of these magnetic moments on the ac and bc planes.

The Fe^{3+} and R^{3+} magnetic moments were also refined from NDP data collected on D1B as a function of temperature. Their thermal variation indicates that 3D magnetic order begins to develop simultaneously, at T_N below ~ 40 K, in both networks for each compound. In general, the magnetic moments of Fe^{3+} increase rapidly when the temperature decreases, and reach their saturation values below 20 K, whereas those of R^{3+} increase more gradually and attain saturation only at lower temperatures, below 10 K. The saturation moments for Dy^{3+} , Tm^{3+} , and Yb^{3+} [6.9(2), 3.5(4), and 1.3(2) μ_B , respectively] are smaller than those expected for the corresponding free ions, namely, 10, 7, and 4 μ_B . The strong reduction is most probably caused by the

Table 8. Magnetic Moments at 1.6 K for R^{3+} and Fe^{3+} in $RFeGe_2O_7$, $R = Y, Pr, Dy, Tm$, and Yb , in Cartesian and Spherical Coordinates

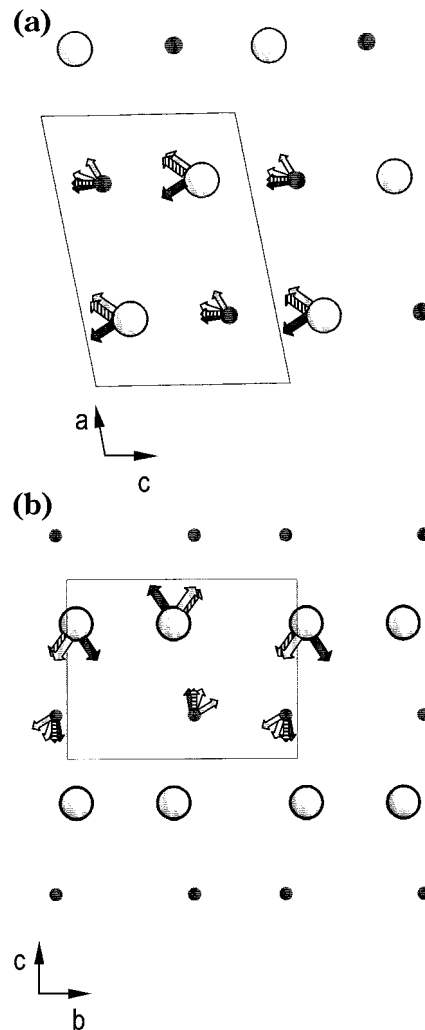
	R						Fe					
	M_x/μ_B	M_y/μ_B	M_z/μ_B	M/μ_B	$\varphi/^\circ$	$\phi/^\circ$	M_x/μ_B	M_y/μ_B	M_z/μ_B	M/μ_B	$\varphi/^\circ$	$\phi/^\circ$
Y							1.2(4)		-3.2(2)	3.64(9)		161.0
Pr	-2.8(3)	1.29(2)	-2.0(4)	2.9(2)	155.4	255.4	-1.2(2)	2.4(2)	-2.2(4)	3.1(3)	115.9	237.9
Dy	-3.9(2)		-6.4(2)	6.9(2)		213.9	-0.7(2)		-4.8(2)	4.8(2)		188.7
Tm	2.2(3)		-2.5(3)	3.5(4)		144.7	3.3(3)		-1.3(3)	3.7(4)		121.5
Yb	0.8(2)		-0.9(1)	1.3(2)		143.6	-0.1(2)		-3.4(1)	3.4(2)		181.0

**Figure 10.** Observed, calculated, and difference neutron diffraction (D1B, ILL) profiles of $DyFeGe_2O_7$ at 1.6 K. The vertical marks correspond to the positions of the allowed Bragg reflections for the crystallographic (first row) and magnetic (second row) structures. The difference curve is plotted at the bottom of the figure.

population changes within the ground R^{3+} state associated with their splitting by crystal-field effects, and, especially for ground Dy^{3+} ($^6H_{15/2}$) and Yb^{3+} ($^2F_{7/2}$), Kramers doublets that are further split by the exchange interaction with the ordered Fe^{3+} subsystem.¹¹ The magnetic moments determined for Fe^{3+} are also smaller than the theoretical value of $5.9 \mu_B$ (high-spin Fe^{3+}), probably because of covalence effects and to quantum spin fluctuations; nevertheless, they are close to the values obtained for the remaining trivalent rare earth iron germanates of the family.^{8,11} Figure 12 shows the thermal behavior of the magnetic moment for $DyFeGe_2O_7$, which was selected because the magnetic moment of Dy^{3+} is the highest among the studied compounds. The large error bars observed around the ordering temperature are due to the small magnetic moments at these temperatures when their order is not complete. Within the temperature range between the establishing of the order and the saturation of the Dy^{3+} magnetic moments, a faster increase, observed as a subtle change in the slope of the curve, is detected around 26 K.

Discussion and Conclusions

From results of $\chi_m(T)$ and NPD measurements on $RFeGe_2O_7$ compounds, it can be assumed that the nature of the low-temperature ordered phase as well as the mechanism for its transition from the room-temperature structure is imposed by existing arrangements of Fe and R cations in the adopted I- or II- $RFeGe_2O_7$ structure. In the first case, whereas, for $LaFeGe_2O_7$, only short-range magnetic fluctuations of the Fe^{3+} magnetic system (isolated FeO_5 units that connect chains of LaO_9 polyhedra) are observed at around 250 K, and consequently no long-range order appears even

**Figure 11.** Projection of the arrangement of magnetic moments of R and Fe onto the (a) ac and (b) bc planes. The large and small spheres represent R and Fe atoms, respectively, and the white, black, gray, and dashed arrows correspond to Y, Dy, Tm, and Yb compounds, respectively.

at low temperatures, in the isostructural $PrFeGe_2O_7$ material, the transition to the magnetically ordered phase is due to $Pr^{3+}-Pr^{3+}$ interactions, which take place at very low temperatures. The magnetic order in the Pr system would induce the ordering of the iron moments, through Pr-Fe interactions, with a simultaneous ordering of both the Pr^{3+} and Fe^{3+} sublattices and the same propagation vector. In short, in this structure, it is the connection between chains of magnetic rare earth RO_9 -tricapped trigonal prisms through FeO_5 that creates the adequate pathway for magnetic interactions between the two kinds of magnetic cations, thus leading to the low-temperature 3D AF ordering of the structure. The magnetic behavior of I- $RFeGe_2O_7$ compounds

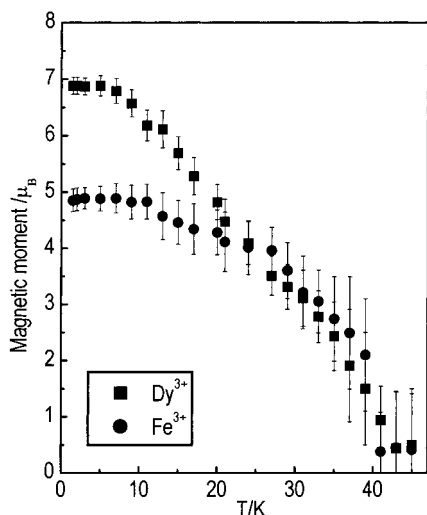


Figure 12. Temperature dependence of the ordered magnetic moments of Fe^{3+} and Dy^{3+} in $\text{DyFeGe}_2\text{O}_7$.

would then be dominated by the paramagnetic rare earth, i.e., the stronger R–R interactions. A similar behavior was very recently observed for magnetic trivalent rare earth copper germanates of the stoichiometry $\text{R}_2\text{CuGe}_4\text{O}_{12}$.¹⁶

In contrast to $\text{LaFeGe}_2\text{O}_7$, the low-temperature phase of YFeGe_2O_7 presents 3D magnetic order. The exchange interaction through FeO_6 octahedra linked in pairs, with Fe–Fe distances of ~ 3.4 Å, allows the existence of the long-range 3D order. For the remaining II– RFeGe_2O_7 compounds, when R is a magnetic rare earth such as Dy, Tm, or Yb, the two magnetic lattices begin to present 3D ordering at the same temperature, around 40 K, and thus, only one irreducible representation is favored in the transition. However, similarly to the behavior described¹⁷ for other systems with magnetic interactions between 4f and 3d ions, the presence of two separate anomalies, with one at $T_1 \approx 40$ K and the more intense one at T_2 , $T_2 < T_1$, as revealed by χ_m vs T curves,

can be attributed to the existence of two different magnetic phase transitions. Nevertheless, analyses of current NPD data indicate that T_N coincides with T_1 and also that no magnetic phase transition or spin reorientation occurs at T_2 . Confirming this fact, earlier high-resolution optical absorption measurements of transitions in the $^4\text{I}_{15/2} \rightarrow ^4\text{I}_{13/2}$ spectral region for Er^{3+} in isostructural $\text{ErFeGe}_2\text{O}_7$ ¹¹ show that the temperature of the magnetic order transition, seen as the temperature for which Kramers doublets are split by the internal magnetic field that originates during the magnetic ordering of the system, absolutely coincides with the value of T_N found from the low-temperature NPD analysis. Moreover, the spectral shapes were found to be identical at both T_1 and T_2 , which indicates the absence of any magnetic transition between the two temperatures. The accordance between independent data sustains the origin of these separate anomalies as being based in Fe–Fe and Fe–R exchange interactions. Below T_N ($= T_1$), the R^{3+} moments become simply polarized under the local effective field arising from ordered Fe^{3+} moments, and the faster increase of the R^{3+} moments below T_2 , visible in Figure 12 and also reported for $\text{TbFeGe}_2\text{O}_7$,⁸ is due to the stronger Fe–R interactions and crystal-field effects¹¹ causing population changes within the R^{3+} ground-state manifolds. It follows that, in contrast with I– RFeGe_2O_7 compounds, R–R interactions are weaker than Fe–R interactions. Finally, the latter interactions in II– RFeGe_2O_7 compounds are highly anisotropic, reflecting the different direction of the anisotropy of the corresponding rare earth constituent. Consequently, although exhibiting the same structure in the ordered state, described by the same B_g irreducible representation, the directions of the moments can be regarded as being either mainly aligned along the c axis ($\text{R} = \text{Y}$, Tb ,⁸ Ho ,¹¹ and Yb) or closer to the a direction ($\text{R} = \text{Er}$ ¹¹ and Tm).

Acknowledgment. The authors acknowledge the financial support of the Spanish DGESIC, Project PB97-1200, and Institut Laue-Langevin for the neutron scattering facilities offered.

CM0111332

(16) Cascales, C.; Fernández-Díaz, M. T.; Monge, M. A. *Chem. Mater.* **2000**, *12*, 3369.

(17) García Matres, E.; García Muñoz, J. L.; Martínez, J. L.; Rodríguez Carvajal, J. *J. Magn. Magn. Mater.* **1995**, *149*, 363.